JOURNAL OF GEOPHYSICAL RESEARCH: SOLID EARTH, VOL. 118, 1–15, doi:10.1002/jgrb.50219, 2013

Radially anisotropic structure beneath the Shikoku Basin from broadband surface wave analysis of ocean bottom seismometer records

A. Takeo,[1] K. Nishida,[1] T. Isse,[1] H. Kawakatsu,[1] H. Shiobara,[1] H. Sugioka,[2]
and T. Kanazawa[3]

Received 1 February 2013; revised 1 May 2013; accepted 9 May 2013.

[1] We have analyzed broadband surface wave data from ocean bottom seismometers deployed in the Shikoku Basin in the northeastern Philippine Sea to determine the radially anisotropic uppermost mantle structure beneath this oceanic basin. We first applied noise correlation method to continuous microseismic records to obtain phase velocities for fundamental-mode and first higher-mode Rayleigh waves and fundamental-mode Love waves at periods of 7–29 s. At longer periods, we applied an array analysis method to teleseismic surface waves to obtain phase velocities of fundamental-mode Rayleigh and Love waves at periods of 29–117 s. Using these broadband phase velocity measurements, we have determined the one-dimensional radially anisotropic structure from the crust to the low velocity zone (LVZ) beneath the Shikoku Basin without assuming a priori structure in the uppermost mantle. The final structural model (SB-RA10) has a high-velocity lid from the Moho to a depth of ~40 km, with an LVZ at greater depths. *S* wave velocities decrease by 6%–10% at a depth range of ~40–70 km. This large decrease in velocity suggests that there is either a large difference in grain size between these layers or indicates the presence of partial melt or water in the LVZ. Furthermore, strong radial anisotropy of 4%–5% ($V_{SH} > V_{SV}$) is observed in the uppermost mantle, which may be stronger in the LVZ.

Citation: Takeo, A., K. Nishida, T. Isse, H. Kawakatsu, H. Shiobara, H. Sugioka, and T. Kanazawa (2013), Radially anisotropic structure beneath the Shikoku Basin from broadband surface wave analysis of ocean bottom seismometer records, *J. Geophys. Res. Solid Earth*, *118*, doi:10.1002/jgrb.50219.

1. Introduction

[2] The seismic low velocity zone (LVZ) exists beneath a high velocity lid (LID) at a depth of ~50–200 km in the uppermost mantle beneath oceanic basins [e.g., *Gutenberg*, 1959; *Press*, 1959]. As the LVZ seems to mark the oceanic asthenosphere, elucidating the seismic structure of the LVZ and LID is essential for understanding plate tectonics. The nature and location of the LVZ has been investigated using dispersion curves of surface waves [e.g., *Dorman et al.*, 1960; *Leeds et al.*, 1974]. Recent surface wave tomographic studies have greatly improved the large scale picture of the lateral variations of the oceanic uppermost mantle, such as the seafloor-age dependence of the LID/LVZ structure [e.g., *Ritzwoller et al.*, 2004; *Maggi et al.*, 2006; *Nettles and Dziewonski*, 2008], but the depth resolution is usually limited to discuss the origin of the LVZ due to the broad depth sensitivity of surface wave velocities (especially at long periods) to the mantle structure.

[3] Body wave reflections and/or conversions are useful in determining the depths of discontinuities, such as the G-discontinuity that is the boundary between the LID and LVZ [e.g., *Revenaugh and Jordan*, 1991; *Kawakatsu et al.*, 2009; *Rychert and Shearer*, 2011], although the spatial coverage is limited by the locations of earthquakes and stations. *Gaherty et al.* [1996] and *Kato and Jordan* [1999] analyzed both body and surface waves and obtained path-average one-dimensional structures with the G-discontinuity beneath the central Pacific and Philippine Sea regions, respectively. These structures have been used to discuss the origin of the LVZ, such as its thermal structure [*Stixrude and Lithgow-Bertelloni*, 2005], grain size variations [*Faul and Jackson*, 2005], and the presence/absence of partial melt [e.g., *Anderson and Sammis*, 1970] of water [*Karato*, 2012]. However, the employed long-path averaging of these studies

---

[1] Earthquake Research Institute, University of Tokyo, Tokyo, Japan.
[2] Institute For Research on Earth Evolution, Japan Agency for Marine-Earth Science and Technology, Yokosuka, Japan.
[3] National Research Institute for Earth Science and Disaster Prevention, Tsukuba, Japan.

Corresponding author: A. Takeo, Earthquake Research Institute, University of Tokyo, 1-1-1, Yayoi, Bunkyo-ku, Tokyo 113-0032, Japan. (akiko-t@eri.u-tokyo.ac.jp)

2169-9313/13/10.1002/jgrb.50219

appears inadequate for evaluating the various models proposed for the origin of the LVZ.

[4] The presence of strong seismic anisotropy (both radial and azimuthal) in the uppermost mantle beneath oceanic basins [e.g., *Forsyth*, 1975] further complicates the situation. A radially anisotropic structure without azimuthal dependence is conventionally introduced to account for the discrepancy between Rayleigh and Love waves and can be understood either as the azimuthal average of more general anisotropic structure [*Anderson*, 1962; *Aki and Kaminuma*, 1963; *Dziewonski and Anderson*, 1981] or the long-period equivalent of fine layering [e.g., *Backus*, 1962]. Recent tomographic studies have shown that the presence of radial anisotropy ($V_{SH} > V_{SV}$) is stronger in the LVZ than in the LID [e.g., *Ekström and Dziewonski*, 1998; *Nettles and Dziewonski*, 2008], which leads to two potential interpretations: the enhancement of lattice preferred orientations (LPO) in the LVZ [e.g., *Podolefsky et al.*, 2004; *Becker et al.*, 2008; *Behn et al.*, 2009], or the presence of pockets or layers of partial melt under shear stress [e.g., *Schlue and Knopoff*, 1976; *Kawakatsu et al.*, 2009]. As far as radial anisotropy is concerned, the usage of body waves is not so effective, as the velocities of nearly vertical propagation *S* waves are close to that of V_{SV} that Rayleigh waves are sensitive [e.g., *Takeuchi and Saito*, 1972]. It is, therefore, essential to analyze Love waves to determine the V_{SH} structure.

[5] Surface waves with periods shorter than 40 s are sensitive to the structure at depths shallower than 50–100 km and important for examining not only the shallow structure but also radial anisotropy at depths of ~100 km through the depth tradeoff [*Bozdag and Trampert*, 2008]. However, over this period range, a seismometer array is required for precisely measuring phase velocities by estimating the effects of ray bending and multipathing [*Forsyth and Li*, 2005]. Such an array is also useful for the ambient noise cross-correlation analysis that extracts the background surface waves in a period range of microseisms [e.g., *Aki*, 1957; *Shapiro and Campillo*, 2004; *Bensen et al.*, 2008; *Nishida et al.*, 2008].

[6] Seismometer array records have been extensively analyzed in the East Pacific Rise (EPR) region, where many ocean bottom seismometers (OBSs) have been deployed. For example, *Dunn and Forsyth* [2003] measured the phase velocity of fundamental-mode Love waves at periods of 4–17 s using local seismic events and obtained a two-dimensional V_{SH} structure. *Forsyth and Li* [2005] and *Weeraratne et al.* [2007] measured the phase velocity of fundamental-mode Rayleigh waves at periods of 18–100 s using teleseismic events and obtained a three-dimensional V_{SV} structure that included azimuthal anisotropy. *Harmon et al.* [2007] and *Yao et al.* [2011] also analyzed both fundamental-mode and first higher-mode Rayleigh waves at periods of 2–30 s by applying the noise correlation method to OBS records. By using phase velocities of Rayleigh waves measured from teleseismic waveforms at longer periods, *Harmon et al.* [2007] and *Yao et al.* [2011] obtained a one-dimensional structure of V_{SV} from the crust to a depth of ~100 km with a depth resolution that was much higher than that in global tomographic studies.

[7] What is now desired and possible by using the state-of-the-art OBS array is to analyze both Rayleigh and Love waves simultaneously in a broadband period range of ~10–100 s to constrain the in situ uppermost mantle structure including radial anisotropy with the depth resolution sufficient to discuss the origin of the LVZ. For the purpose of this study, we analyze records from the broadband OBS array deployed in the Shikoku Basin (SB) in the Philippine Sea region [*Shiobara et al.*, 2009]. This offers one of the best quality OBS data sets (e.g., long-period Love waves are well-observed for moderate size earthquakes [*Isse et al.*, 2010]), nevertheless, the high noise level of OBS measurements still makes the analyses difficult. Therefore, we first develop techniques to deal with such noisy data for broadband dispersion analyses and then solve for an in situ local average property beneath the array. With the currently available data set, we only solve for the radial anisotropy but not for the azimuthal one nor for their lateral variations, which are left for the future work with denser and/or large scale arrays.

2. Study Area and Data

[8] During the Stagnant Slab Project, broadband OBSs (BBOBSs) [*Kanazawa et al.*, 2009] were deployed from 2005 to 2008 in and around the Philippine Sea [*Shiobara et al.*, 2009] (Figure 1). One year observations were repeated once, twice, or three times at each of the 17 stations. The BBOBSs were equipped with Guralp CMG-3T sensors with a flat velocity response from 0.02 to 360 s. The noise spectra of a BBOBS shown in Figure 1 suggest that the noise level of the vertical component is comparable to that of on-land records, but the noise level of the horizontal component is higher. Given that the noise level strongly depends on the site, the component, and the observation period, the employment of proper methods of seismic data analysis appears to be essential.

[9] *Nakamura and Shibutani* [1998] first performed regional surface-wave tomography for obtaining three-dimensional V_{SV} structure beneath the Philippine Sea region. *Isse et al.* [2009] used BBOBS records as well as on-land records and improved the lateral resolution of the V_{SV} structure. Their study revealed three strong, slow anomalies in the mantle wedge along the Izu-Bonin (Ogasawara)-Mariana arc (IBM). *Isse et al.* [2010] also identified azimuthally and radially anisotropic structure in the same region, and showed that the fast direction of azimuthal anisotropy is consistent with ancient seafloor spreading at depths shallower than 100 km and with the current plate motion at greater depths. However, these previous studies only analyzed surface waves at periods longer than 30 s and, as such, the depth resolution of their obtained structures at shallow depths is limited.

[10] In the present study, we focused on obtaining a robust one-dimensional structure in order to compare with thermal models for oceanic basins to discuss the origin of the LVZ. The arrays of BBOBSs were deployed in the SB (seven stations) and Pacific Basin (five stations). We only used data from the SB, as the data from the Pacific Basin are not suited for our analysis due to high noise levels. The SB is a back-arc basin in the northeastern part of the Philippine Sea Plate that formed at 15–30 Ma [*Okino et al.*, 1999], and is surrounded by the Nankai Trough, IBM, Kyusyu–Palau ridge, and Parece–Vela basin. The Pacific Plate is subducting beneath the Philippine Sea Plate, whereas the Philippine Sea

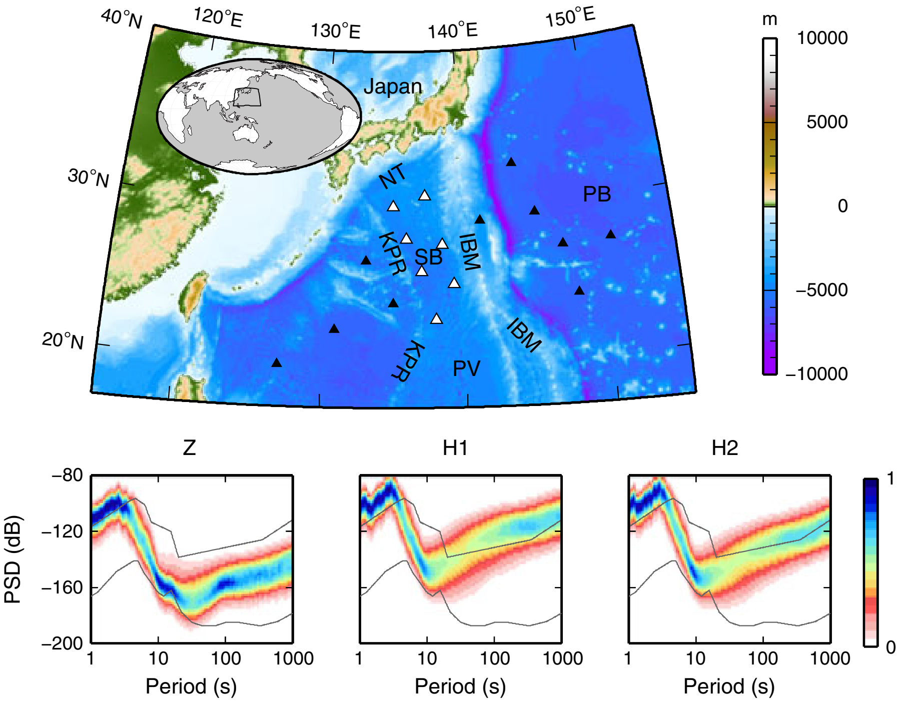

Figure 1. (top) Topographic map and BBOBS stations of the Stagnant Slab Project (triangles). Open triangles show stations in the SB used in this study. IBM, Izu–Bonin–Mariana arc; KPR, Kyushu–Palau ridge; NT, Nankai Trough; PB, Pacific Basin; PV, Parece–Vela basin; SB, Shikoku Basin. (bottom) Colors show the probability density of acceleration power spectrum density (PSD) of vertical (Z) and horizontal (H1 and H2) components at a typical station normalized to the maximum probability density. The gray lines show New Low and High Noise Models [*Peterson*, 1993].

Plate itself is subducting beneath southwest Japan. Although the tectonic setting of the SB is complicated, the uppermost mantle structure beneath the SB is expected to be similar to that in other oceanic basins, as the SB has normal oceanic crust [*Nishizawa et al.*, 2011].

3. Phase Velocity Measurements

[11] We used the two array analysis methods for measuring broadband phase velocities of Rayleigh and Love waves (Table 1). Noise correlation analysis was conducted at periods of 7–29 s and teleseismic waveform array analysis was undertaken at periods of 29–117 s. In applying both methods, we assume that the effects of lateral heterogeneity and azimuthal anisotropy are small, and measure average phase velocities within seismic array in order to constrain the average structure beneath the SB.

3.1. Uniqueness of Surface Waves in Oceanic Regions

[12] Before describing the phase velocity measurements, we summarize the nature of surface wave dispersions and their sensitivity to the mantle structure in oceanic regions. The sensitivity of phase velocity (c) at a period of T to a parameter p at a depth of z, $K_p(z, T)$, is defined as follows:

$$\frac{\Delta c(T)}{c(T)} = \int \left[\sum_p K_p(z,T) \frac{\Delta p(z)}{p(z)} \right] \mathrm{d}z, \tag{1}$$

where Δc is the perturbation of the phase velocity when Δp is added to the parameter p. Figure 2 shows phase velocities

Table 1. Summary of Phase Velocity Measurements

	Noise Correlation Analysis			Teleseismic Waveform Analysis	
Component (γ)	vertical (Z)	radial (R)	transverse (T)	vertical (Z’)	transverse (T’)
Wave type	Rayleigh	Rayleigh	Love	Rayleigh	Love
Mode	fundamental	1st higher	fundamental	fundamental	fundamental
Period	14–29 s	7–11 s	7–20 s	29–117 s	29–59 s
Number[a]	(9,15,6)	(6,9,6)	(6,9,6)	137	29
Number[b]	4	5	7	7	3
Number[c]	6	5	10	10	6

[a] Numbers of pairs for the first, second, and third years during the observation period for noise-correlation analysis. Numbers of events for teleseismic waveform array analysis.

[b] Numbers of spline functions used for measuring phase velocities.

[c] Numbers of measurements used for structural inversion.

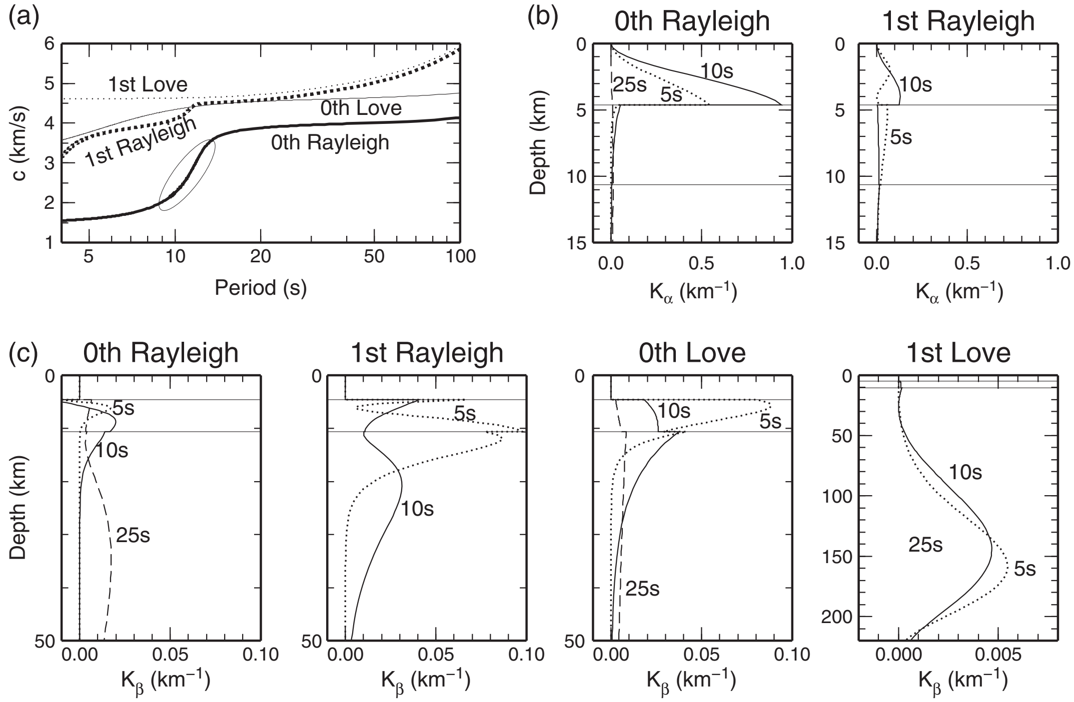

Figure 2. (a) Phase velocities of the fundamental (0th) and first higher modes of surface waves for the modified PREM. The sudden phase velocity decrease marked by ellipse corresponds to the transition of modal energy from solid to ocean. (b, c) Sensitivities of phase velocities to *P* wave and *S* wave velocities (K_α and K_β, respectively). The two lines in each panel show the depths of the seafloor and Moho.

and their sensitivities to *P* and *S* wave velocities for a model based on PREM [*Dziewonski and Anderson*, 1981], where the thickness of the ocean is changed from 3.0 to 4.6 km, and the thickness of the crust is reduced from 22 to 6 km. We used the Fortran package DISPER80 [*Saito*, 1988] with the physical dispersion [*Kanamori and Anderson*, 1977] to calculate the phase velocities of Rayleigh and Love waves from eigenperiods of spheroidal and toroidal modes, respectively.

[13] The difference between oceanic and continental regions is reflected in the sudden decrease of phase velocity for fundamental-mode Rayleigh waves at a period of ∼14 s. This decrease corresponds to the transition of modal energy from the solid to the ocean, and the period of the phase velocity drop is related to the ocean depth [*Ewing et al.*, 1957]. At shorter periods, the fundamental-mode Rayleigh wave has sensitivity to *S* wave velocity in the crust, but the sensitivity to *S* wave velocity (Figure 2c) is smaller than that to *P* wave velocity in the ocean (Figure 2b). In contrast, the first higher-mode Rayleigh wave in oceanic model corresponds to a fundamental-mode wave in an ocean-free model. Both modes need to be considered and analyzed to obtain the V_{SV} structure in the uppermost mantle. *Yao et al.* [2011] referred to these waves as Scholte-Rayleigh waves by considering them to be related to the presence of a fluid-solid interface. For the sake of simplicity, in this paper we refer to these waves as Rayleigh waves.

3.2. Noise Correlation Analysis

[14] At periods shorter than 29 s, we extracted the background surface wave propagation between pairs of stations by cross-correlating continuous records of ambient noise [*Aki*, 1957]. Processing was performed in the frequency domain. The whole data set was first divided into segments of 1638 s with overlaps of 819 s. After discarding any segments containing earthquake signals, a Fourier spectrum ($f_{j,\gamma}(\omega)$) was calculated for each segment, where *j* is the station number, γ is the type of component, and ω is the angular frequency. We used three types of components: vertical (γ=Z), radial (γ=R), and transverse (γ=T). For each observation period (1 year), we then took ensemble averages of the cross spectrum ($S^{\text{raw}}_{i,\gamma}(\omega)$) between *i*th pairs of stations (*j*th and *k*th stations) as follows:

$$S^{\text{raw}}_{i,\gamma}(\omega)=\frac{\left\langle w_{i,\gamma}(\omega)\cdot f_{j,\gamma}(\omega)\cdot f^{*}_{k,\gamma}(\omega)\right\rangle}{\left\langle w_{i,\gamma}(\omega)\right\rangle}, \tag{2}$$

where $w_{i,\gamma}$ is a weighting term obtained by

$$w_{i,\gamma}=\frac{1}{|\tilde{f}_{j,\gamma}|}\cdot\frac{1}{|\tilde{f}_{k,\gamma}|}. \tag{3}$$

The normalized amplitude is $|\tilde{f}_{j,Z}| = |f_{j,Z}|$ for the vertical component and $|\tilde{f}_{j,T}| = |\tilde{f}_{j,R}| = \sqrt{(|f_{j,T}|^2+|f_{j,R}|^2)/2}$ for the two horizontal components. The definition of cross spectrum in equation (2) is similar to the conventional definition of cross spectrum:

$$S^{\text{raw}}_{i,\gamma}(\omega)=\left\langle \frac{f_{j,\gamma}}{|\tilde{f}_{j,\gamma}|}\cdot\frac{f^{*}_{k,\gamma}}{|\tilde{f}_{k,\gamma}|}\right\rangle=\left\langle w_{i,\gamma}\cdot f_{j,\gamma}\cdot f^{*}_{k,\gamma}\right\rangle, \tag{4}$$

which is called spectrum normalization or whitening [*Bensen et al.*, 2007]. If the continuous records only contain signals (background surface waves), then the spectrum

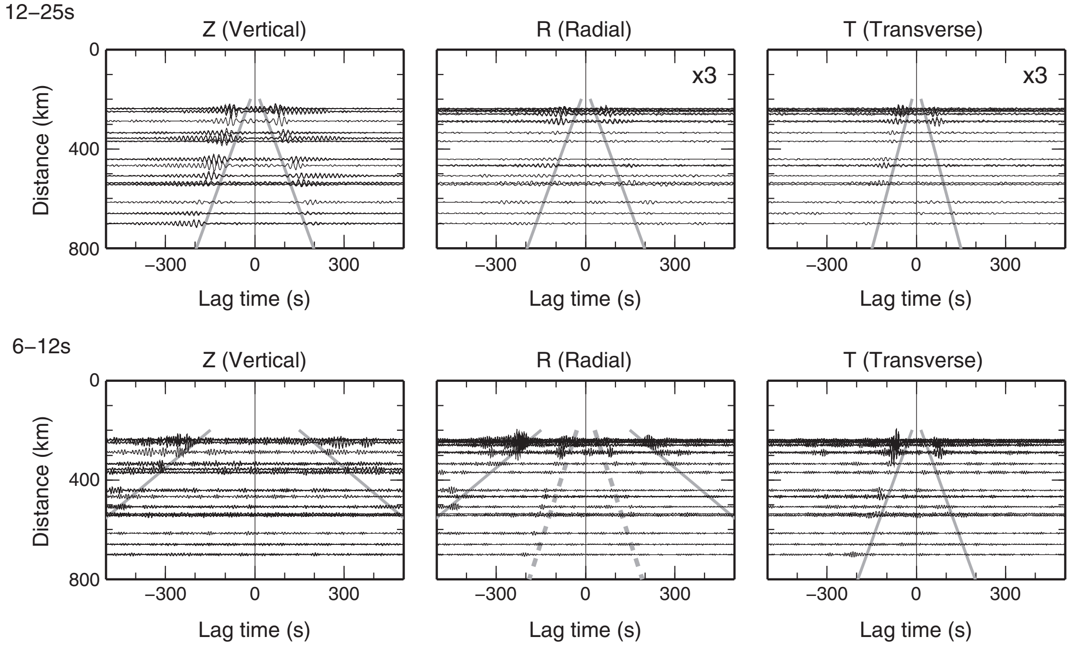

Figure 3. CCFs with (top) 12–25 s and (bottom) 6–12 s band-pass filters. Solid and broken gray lines mark the fundamental mode and first higher mode, respectively. We multiplied each cross spectrum by $\langle w_{i,\gamma}(\omega)\rangle$ before calculating the CCF for reducing the CCF amplitude with large uncertainties (Appendix A). The amplitude of the two horizontal components (6–12 s) is exaggerated by a factor of 3 as compared with the vertical component.

normalization is equivalent to the deconvolution of source spectrum [*Nakahara*, 2006]. If the noise level is much higher than the signal level, as is the case with the BBOBS records used in this study, then the amplitude of each Fourier spectrum reflects the noise level. In this latter case, the normalization is not equivalent to the source deconvolution, but simply suppresses the contribution of noisy data. When we use equation (4), however, the amplitude of the cross spectrum becomes smaller for the pair of stations with the higher noise levels. We therefore use equation (2) to compensate for the effect of weighting. The uncertainty of a cross spectrum is proportional to $\langle w_{i,\gamma}\rangle^{-1}$, which is approximately equal to the product of noise levels at *j*th and *k*th stations (Appendix A).

[15] Figure 3 shows cross-correlation functions (CCFs) or inverse-Fourier transformed cross spectra for two period ranges. Multiple modes of surface waves can be recognized in each component: (1) fundamental-mode Rayleigh waves (6–25 s) in vertical components; (2) both first higher-mode (6–12 s) and fundamental-mode (6–25 s) Rayleigh waves in radial components; and (3) fundamental-mode Love waves (6–25 s) in transverse components. We applied a group-velocity filter to each CCF to extract major modes (Table 1) while suppressing noise and a minor fundamental-mode Rayleigh wave in radial components at periods of 6–12 s. The fundamental-mode Rayleigh wave at periods shorter than 14 s was not analyzed, as it mainly represents the *P* wave velocity in the ocean (Figure 2b). Although each CCF reflects the structure between a station pair under the assumption of homogeneous source distribution [e.g., *Tromp et al.*, 2010; *Nishida*, 2011], the signal-to-noise ratio of a CCF does not allow individual phase velocities to be determined, particularly for horizontal components.

[16] Therefore, we measured the average phase velocity in the area of the array using the spatial auto-correlation method of *Aki* [1957]. Assuming a laterally homogeneous structure and a homogenous source distribution, the cross spectrum for the vertical component (γ=Z) is given by

$$S^{\mathrm{the}}_{i,\gamma}(\omega, c, a) = aJ_0\left(\frac{\omega d_i}{c}\right), \tag{5}$$

where $a(\geq 0)$ is a constant indicating the source intensity, J_0 is the 0th Bessel function, d_i is the distance between stations in the *i*th station pair, and c is the phase velocity. For a wavelength much shorter than the interstation distance ($c/\omega << d_i$), we can ignore transverse components of Rayleigh waves and radial components of Love waves. The cross spectrum for the horizontal components (γ=R,T) is then given by

$$S^{\mathrm{the}}_{i,\gamma}(\omega, c, a) = a\left[J_0\left(\frac{\omega d_i}{c}\right) - J_1\left(\frac{\omega d_i}{c}\right) / \left(\frac{\omega d_i}{c}\right)\right], \tag{6}$$

where J_1 is the 1st Bessel function.

[17] Using equation (5) and (6), we determined the average phase velocity in the area of the array in two steps. In the first step, we estimated the source intensity ($a = a^{\mathrm{opt}}_{\gamma}(\omega, c)$) that minimizes the misfit between the data and prediction:

$$F_{\gamma}(\omega, c, a) = \sum_i \langle w_{i,\gamma}\rangle^2 \left[S^{\mathrm{data}}_{i,\gamma} - S^{\mathrm{the}}_{i,\gamma}\right]^2, \tag{7}$$

with the least squares method for each angular frequency (ω) and assumed phase velocity (c). As the imaginary parts

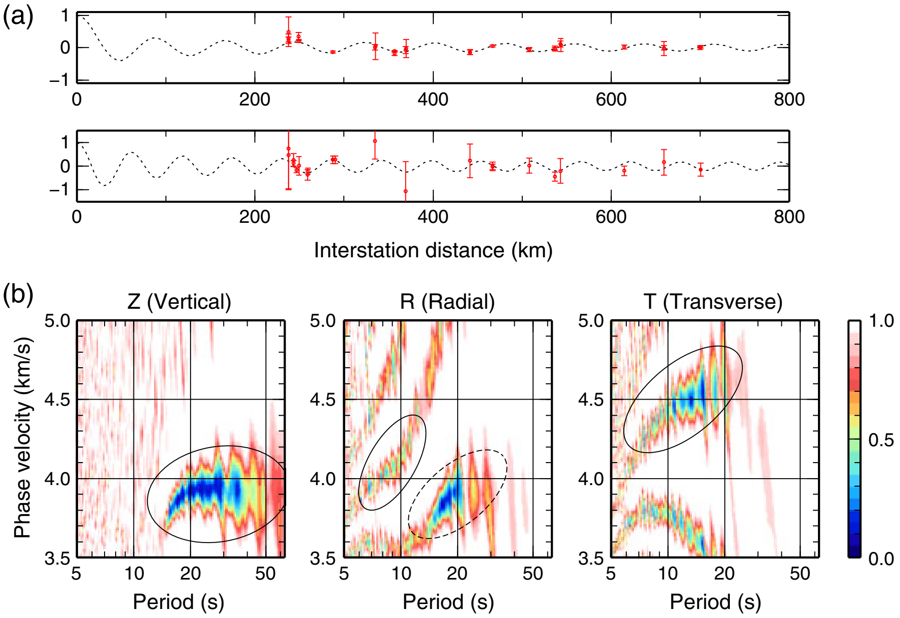

Figure 4. (a) Examples of fitting between the obtained cross spectra and the theoretical equation normalized by the theoretical value at 0 km. Figure 4a (top) shows the vertical component for $T = 20$ s and $c = 3.92$ km/s. Figure 4a (bottom) shows the transverse component for $T = 12$ s and $c = 4.50$ km/s. The error bar sizes are proportional to the uncertainty of each cross spectrum $(1/\langle w_{i,\gamma}\rangle)$ (Appendix A). (b) Misfit between the data and theoretical equation as a function of T and c. We measured phase velocities in the signal marked by the solid ellipses. The phase velocities of the fundamental-mode Rayleigh wave are shown as a broken ellipse in the radial components but are not used in this study.

of the cross spectra (time-asymmetric components) mainly reflect a non-isotropic source distribution [e.g., *Ekström et al.*, 2009; *Weaver et al.*, 2009], we used the real parts of the cross spectra after group velocity filtering in the time domain as the data $S^{\text{data}}_{i,\gamma}(\omega)$. The weighting term $(\langle w_{i,\gamma}\rangle^2)$ accounts for the difference in data uncertainties (Appendix A). Figure 4a shows examples of fitting for both vertical and transverse components, and Figure 4b shows the misfit normalized by the weighted summation of square of the data $(F_\gamma(\omega, c, a^{\text{opt}})/\sum_i \langle w_{i,\gamma}\rangle^2 [S^{\text{data}}_{i,\gamma}]^2)$, as a function of period $(T = 2\pi/\omega)$ and assumed phase velocity. Given that the variation in interstation distances is limited, several phase velocities can potentially fit the data as shown by the different curves of high variance reduction in Figure 4b. We identified appropriate curves (solid ellipses in Figure 4b) by comparing them with phase velocities for the modified PREM model (Figure 2a). Although it is possible to recognize the phase velocities of fundamental-mode Rayleigh waves at periods of 14–30 s from radial components (dashed ellipse in Figure 4b), we measured the phase velocities from vertical components, because the signal-to-noise ratio is better for vertical components.

[18] In the second step, we expressed the phase velocity using B-spline functions $(g_l(\omega))$ and determined coefficients for each function (p_l) by minimizing residuals in a certain frequency range:

$$F'_\gamma(\mathbf{p}) = \sum_{\omega} F_\gamma\left(\omega, c(\omega), a^{\text{opt}}_\gamma(\omega, c(\omega))\right), \tag{8}$$

where $\mathbf{p} = (p_1, p_2, \cdots)$ and $c(\omega) = \sum_l p_l g_l(\omega)$. Given the differences in resolution between component types, the knot interval of the B-spline functions is 0.01 Hz for the vertical component and 0.02 Hz for the two horizontal components. Given this is a nonlinear problem, we used the simulated annealing method of *Ingber* [1989] for optimization. The measurement error is estimated using the bootstrap method [*Efron*, 1979], where 100 dispersion curves $(c^1_\gamma(\omega), c^2_\gamma(\omega), \cdots, c^{100}_\gamma(\omega))$ are estimated for each of the 100 bootstrap samples. A bootstrap sample is the aggregate of station pairs randomly selected from all station pairs allowing for overlaps. We defined the measurement error $(c^{\text{err}}_\gamma(\omega))$ as the standard deviation of 100 dispersion curves. Figure 5 shows the optimal phase velocity curve $(c^{\text{obs}}_\gamma(\omega))$ and the error range $(\bar{c}_\gamma(\omega) \pm c^{\text{err}}_\gamma(\omega))$, where $\bar{c}_\gamma(\omega) = \sum_l c^l_\gamma(\omega)/100$ is the average value taken from the 100 dispersion curves obtained using the bootstrap method.

[19] In the measurement procedure, we assumed a homogeneous source distribution and structure, which may induce bias to the phase velocity measurements. The CCFs shown in Figure 3 indicate that the source distribution is anisotropic. The larger amplitude of the negative lag time as compared with that of positive lag time indicates that the amplitude of the source coming from the northwest, west, or southwest is larger than those coming from the opposite directions. The effect of heterogeneous source distribution can be evaluated by expanding the azimuthal dependence of sources by the Fourier series [*Cox*, 1973; *Weaver et al.*, 2009]. We removed the effect of Fourier components with odd orders by only using the real component of each cross spectrum [*Ekström et al.*, 2009; *Weaver et al.*, 2009]. We minimized the effect of Fourier components with even orders by using station pairs with different azimuths [*Nakahara*, 2006]. We also consider

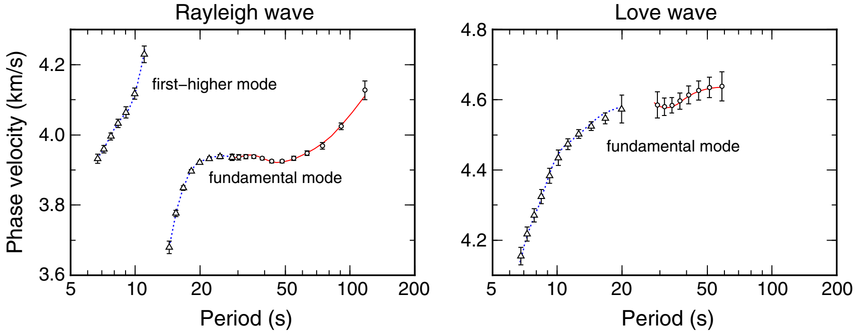

Figure 5. Phase velocities of surface waves measured by noise correlation (triangles and blue dashed lines) and teleseismic waveform array analysis (circles and red solid lines). The curves show measurements from all the data (c_γ^{obs}). Marker symbols with error bars show the uncertainty range ($\bar{c}_\gamma \pm c_\gamma^{\mathrm{err}}$) estimated by the bootstrap method.

the effect of inhomogeneous structure to be small, given that the wavelength is shorter than the interstation distances [*Yao and van der Hilst*, 2009]. In addition, our estimation of measurement error includes the uncertainty related to the lateral heterogeneity within the array because each CCF mainly reflects structure between the stations, and we estimated the error by randomly selecting CCFs. If the structure and the source of ambient noise were laterally homogeneous, the measurement error only reflects the effect of noise in CCFs and becomes smaller than the values estimated in this study.

[20] The period range of precise phase velocity measurements is limited to 7–29 s for Rayleigh waves and 7–20 s for Love waves due to the lower signal-to-noise ratio of CCFs at shorter and longer periods. At shorter periods, the signal may be reduced by scattering due to lateral heterogeneity in the crust beneath the SB [*Nishizawa et al.*, 2011], whereas the signal-to-noise ratio at longer periods is low due to the high noise levels of the BBOBSs (Figure 1). Therefore, at long periods, we used surface waves originating from large teleseismic events.

3.3. Teleseismic Waveform Array Analysis

[21] At periods longer than 29 s, we measured phase velocities of surface waves derived from teleseismic events with moment magnitudes larger than *Mw* 5.5, focal depths shallower than 200 km, and great-circle distances greater than 3000 km. Although the effect of multipathing is small in this long period range [*Forsyth and Li*, 2005], the effect of ray bending cannot be neglected. We corrected for the effects of ray bending by determining the back azimuth of incoming surface waves using the array of BBOBSs. For each event E, we selected 819 s long surface wave records with signal-to-noise ratios higher than 10. The signal amplitude was estimated from the peak of the envelope function, and the noise amplitude was estimated from the root mean square amplitude of 800 s-long records 2 h after the origin time of the event. Figure 6 shows an example of Love wave propagation recorded by the BBOBSs.

[22] We measured average phase velocities using these waveforms with a two-step method. First, we estimated the phase velocity ($c = \sum_l p_l g_l(\omega)$) and the perturbation of incident direction from the great circle ($\theta = \sum_l q_l g_l(\omega)$) for each component ($\gamma$) and each event ($E$) by maximizing the average of cross-correlation coefficients (A) defined as follows:

$$A_\gamma^E(\mathbf{p},\mathbf{q}) = \frac{1}{N_\gamma^E} \sum_{i=1}^{N_\gamma^E} \frac{\sum_\omega \mathcal{R}\mathrm{e}[f_{j,\gamma} \cdot f_{k,\gamma}^{*} \cdot e^{i\Delta\phi_i(\omega,c,\theta)}]}{\sqrt{\sum_\omega |f_{j,\gamma}|^2}\sqrt{\sum_\omega |f_{k,\gamma}|^2}}, \qquad (9)$$

where $\mathcal{R}\mathrm{e}$ is the real component, $f_{j,\gamma}(\omega)$ is the Fourier spectrum for the jth station, N_γ^E is the number of station pairs, and $g_l(\omega)$ is a lth B-spline function. The phase difference between the ith pair of the stations (jth and kth stations), $\Delta\phi_i$, is estimated using the coordinate system proposed by *Forsyth and Li* [2005] with that assuming a propagation of one plane wave in local coordinates (x, y), where $x = x' - x'_0$, and x' is the great circle distance between source and point, x'_0 is the great circle distance between source and reference station, and y is the small circle distance from the point to the great circle connecting the source and the reference station. In this coordinate system, the phase difference between the ith pair of stations is given by

$$\Delta\phi_i(\omega, c, \theta) = \frac{\omega(r_j - r_k)}{c}, \qquad (10)$$

where $r_j = \sqrt{x_j^2 + y_j^2}\cos(\tan^{-1} y_j/x_j - \theta)$, and (x_j, y_j) are the coordinates of the jth station. Using equations (9)

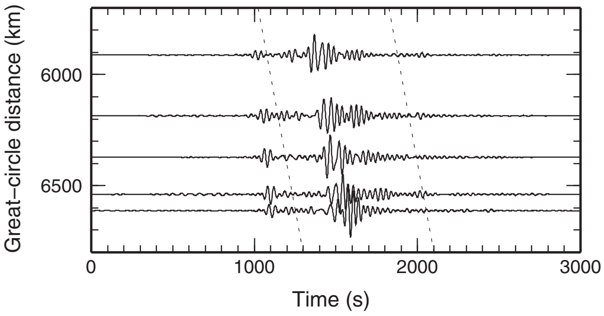

Figure 6. An example of teleseismic Love wave propagation at periods of 29–59 s recorded by BBOBSs for an event with a moment magnitude of 7.3 that occurred at 12:46 on 9 April 2008 (UT). Dashed lines mark the time interval used for analysis.

and (10), we obtain the optimal phase velocity ($c = c^E_\gamma = \sum_l p^E_{l,\gamma} g_l(\omega)$) and optimal incident direction ($\theta = \theta^E_\gamma = \sum_l q^E_{l,\gamma} g_l(\omega)$) for each component ($\gamma$) and each event ($E$). We selected events whose average cross-correlation coefficient ($A^E_\gamma(\mathbf{p}^E_\gamma, \mathbf{q}^E_\gamma)$) was larger than 0.7 for the next step.

[23] In the second step, we searched for the optimal phase velocity curve ($c_\gamma(\omega) = \sum_l p_l g_l(\omega)$) that maximized the summation of cross-correlation coefficients:

$$A^{\mathrm{all}}_\gamma(\mathbf{p}) = \sum_E N^E_\gamma A^E_\gamma\left(\mathbf{p}, \mathbf{q}^E_\gamma\right) \qquad (11)$$

where the incident direction is fixed by the optimal value for each event ($\theta^E_\gamma = \sum_l q^E_l g_l(\omega)$) obtained in the first step. Figure 5 shows phase velocities of fundamental-mode Rayleigh and Love waves obtained from the vertical ($\gamma = Z'$) and transverse ($\gamma = T'$) components, respectively. The number of available events for Love waves ($n = 29$) is smaller than that for Rayleigh waves ($n = 137$) due to the higher noise level of the horizontal-component records. Figure 5 also shows the range of errors estimated by the bootstrap method, where the bootstrap sample was constructed using a randomly selected aggregate of events that allowed overlaps. The errors for Rayleigh waves are much smaller than those for Love waves. The phase velocity of Rayleigh waves at a period of 29 s is consistent with that determined by the noise correlation analysis.

4. 1-D Structural Inversion

[24] Using the phase velocities determined in the previous section, we investigated the one-dimensional radially anisotropic structure beneath the SB.

4.1. Model Parameters

[25] Radially anisotropic media can be described by eight parameters: density, attenuation coefficients for *P* and *S* waves, *P* wave velocity (V_{PH}), *S* wave velocity (V_{SV}), and three anisotropic parameters ($\phi = V^2_{PV}/V^2_{PH}$, $\xi = V^2_{SH}/V^2_{SV}$, and η) [e.g., *Takeuchi and Saito*, 1972]. V_{PV} and V_{PH} denote the velocities of vertically and horizontally propagating *P* waves, respectively, and V_{SV} and V_{SH} are the velocities of horizontally propagating *S* waves with vertical and horizontal polarizations, respectively. The parameter η affects the velocities of *P* and *S* waves with incident angles between 0° and 90°. The phase velocities of Rayleigh waves are largely controlled by variations in V_{SV}, with the phase velocities of Love waves being mainly controlled by variations in V_{SH}. The phase velocity of a fundamental-mode Love wave has a high sensitivity to shallow depths even at long periods, whereas the phase velocity of Rayleigh waves has a high sensitivity to deeper depths at longer periods (Figure 2c). The resolution of V_{SV} is thus higher than that of V_{SH} at depths greater than ~50 km.

[26] Therefore, we estimated V_{SV} in each of the 10 layers from the Moho to a depth of 220 km and estimated *S* wave anisotropy ($\delta V = V_{SH}/V_{SV} - 1$) assuming a constant value of δV. In addition, we estimated the depth of the ocean and V_S in three crustal layers, assuming no anisotropy in these layers. Although other parameters have a slight influence on the phase velocities of Rayleigh and Love waves, independent estimation of these parameters is difficult. We constrained the *P* wave velocity ($V_P = (V_{PV} + V_{PH})/2$) in the mantle to be 1.73 times larger than the *S* wave velocity ($V_S = (V_{SV} + V_{SH})/2$) based on results by an experimental study [*Anderson and Bass*, 1984] and a refraction survey in NW Pacific [*Shinohara et al.*, 2008]. Two anisotropic parameters (ϕ and η) were scaled to the *S* wave anisotropy ($\xi = (\delta V + 1)^2$). The relationships between the three anisotropic parameters have previously been obtained by assuming that LPO is responsible for the anisotropy [*Montagner and Anderson*, 1989; *Becker et al.*, 2008]. We obtained a different scaling by assuming that anisotropy is related to the presence of melt layers (Appendix B), but the difference between the relationships is small for the intensity of anisotropy (δV) lower than 10%. We used the scaling given by *Gung et al.* [2003] based on the work of *Montagner and Anderson* [1989] ($\phi = \xi^{-1.5}$ and $\eta = \xi^{-2.5}$), given that is closer to the mean values determined using the three different relationships. The *P* wave velocity and density in the crustal layers were estimated by using their relationship with *S* wave velocity in the oceanic crust given by *Christensen and Salisbury* [1975]. Other parameters are fixed to the PREM model, including mantle density, attenuation coefficients, and structure deeper than 220 km [*Dziewonski and Anderson*, 1981]. Table 2 summarizes the values used in the initial structure.

Table 2. Variables Used During Modeling of the Initial Structure

	Ocean	Crust			Mantle
Number of Layers	1	3			8
Thickness of layer (km)	4.64	2	2	2	10–70
ρ (g/cc)	1.02	2.3	2.8	3.1	3.3
V_P (km/s)	1.5	3.9	5.6	6.9	7.8
V_S (km/s)	0.0	2.0	3.0	3.7	4.5

4.2. Optimization Method and Results

[27] We again used the simulated annealing method to search for optimal model parameters that led to a small misfit function. The misfit is defined by

$$E = \sqrt{\sum_{\gamma,\omega}\left[\frac{\bar{c}_\gamma(\omega) - c^{syn}_\gamma(\omega)}{c^{\mathrm{err}}_\gamma(\omega)}\right]^2 \Big/ \sum_\gamma N_\gamma}, \qquad (12)$$

where N_γ is the number of measurements for the component γ, $\bar{c}_\gamma(\omega)$ is the bootstrap average of the measured phase velocity, $c^{\mathrm{err}}_\gamma(\omega)$ is the error on the phase velocity measurements, and $c^{syn}_\gamma(\omega)$ is the phase velocity calculated by DISPER80 [*Saito*, 1988] using the model parameters. The frequency interval is constant on a log scale. To reduce the uncertainty related to the trade-off between adjacent layers, we introduce a smoothing term to the misfit function and minimize the summation:

$$E' = E + \epsilon_{\mathrm{sv}} R_{\mathrm{sv}}, \qquad (13)$$

$$R_{\mathrm{sv}} = \sum_{i=1}^{N-1}\left(V^{i+1}_{SV} - V^{i}_{SV}\right)^2, \qquad (14)$$

where ϵ_{sv} is a constant, V^i_{SV} is V_{SV} in the ith layer and $N = 10$ is the number of layers. We evaluated the model uncertainty using dispersion curves obtained by the bootstrap method where 100 dispersion curves ($c^l_\gamma(\omega), (l = 1, \cdots, 100)$) were

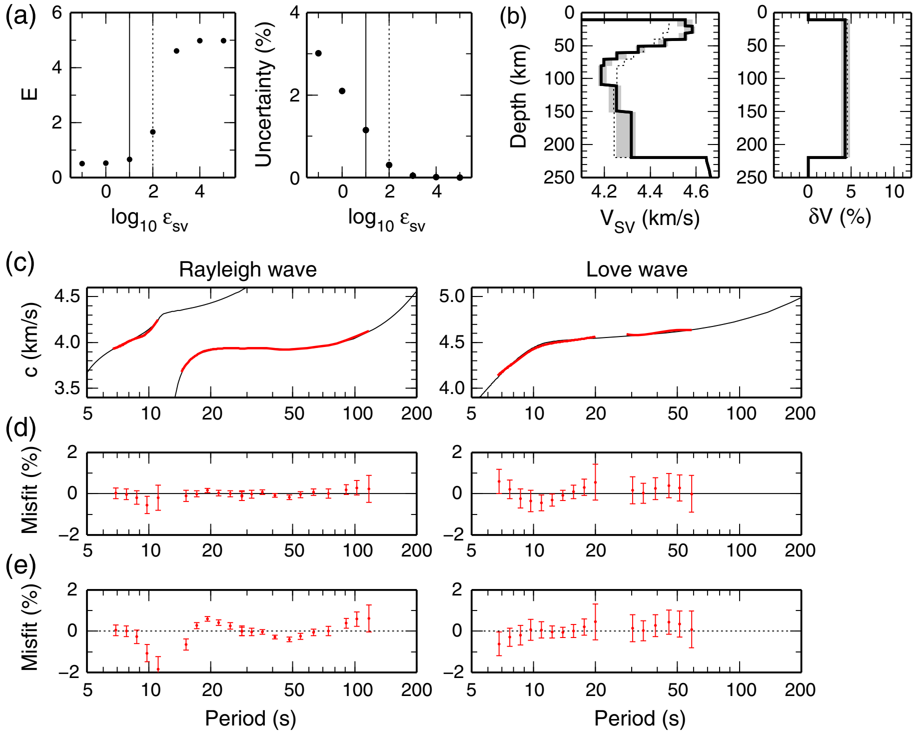

Figure 7. (a) Minimum misfit function (E) and the uncertainty of V_{SV} averaged for 10 layers as a function of $\epsilon_{\rm sv}$. (b) Solid lines show our final model (SB-RA10) corresponding to $\epsilon_{\rm sv} = 10$ at a frequency of 1 Hz. The depth of 0 km corresponds to the ocean surface. Gray areas show the model uncertainty. Broken lines show SB-RA100, which is a smoother structure corresponding to $\epsilon_{\rm sv} = 100$. (c) Phase velocities of SB-RA10 (thin black line) and measurements (thick red line). (d) Misfit between measurements and phase velocities of SB-RA10. (e) Misfit between measurements and phase velocities of SB-RA100.

obtained for each component and method ($\gamma = Z, R, T, Z', T'$; Table 1) as described in the previous section. We searched for the lth model by using the combination of lth dispersion curves (c^l_Z, c^l_R, c^l_T, $c^l_{Z'}$, and $c^l_{T'}$) in the place of average phase velocities ($\bar{c}_\gamma$) in equation (12). For each layer, we then discarded the uppermost and lowermost five values from the 100 values and define this 90% confidence interval range as the model uncertainty.

[28] Figure 7a shows the misfit function (E) and the average of V_{SV} uncertainties in 10 layers as a function of $\epsilon_{\rm sv}$. The misfit function is almost constant for $\epsilon_{\rm sv}$ less than 10, and the uncertainty increases as $\epsilon_{\rm sv}$ decreases. This result means that the fitting does not improve, but the model uncertainty increases for $\epsilon_{\rm sv}$ less than 10. The optimal $\epsilon_{\rm sv}$ value is equal to or larger than 10. The solid lines in Figure 7b show the model corresponding to $\epsilon_{\rm sv} = 10$ (SB-RA10), the radially anisotropic structure beneath the SB. The phase velocities of model SB-RA10 show excellent agreement with the phase velocity measurements as shown in Figure 7d. However, we obtain a smoother model (SB-RA100; broken lines in Figure 7b) if we choose $\epsilon_{\rm sv} = 100$, but the phase velocities of model SB-RA100 do not fit the phase velocity measurements as shown in Figure 7e. We therefore chose $\epsilon_{\rm sv} = 10$ as the final value and SB-RA10 as our preferred final model.

[29] For model SB-RA10, V_{SV} is 4.5–4.6 km/s at a depth range of 10–40 km, decreases by 6%–10% over depths of 40–70 km, becomes 4.15–4.25 km/s at depths of 70–110 km, and slightly increases at greater depths. These results indicate that a low velocity zone (LVZ) exists at depths greater than ~50 km, and that a high velocity LID exists at shallower depths. The thickness of the LID is difficult to define from these results due to a gradual velocity decrease at depths of 40–70 km. We later consider the depth and sharpness of the boundary between the LVZ and LID. The intensity of anisotropy ($V_{SH} > V_{SV}$) is estimated to be 4%–5%. While the assumption of constant anisotropy appears to fit the phase velocity measurements (Figure 7d), we will also subsequently discuss possible variations of anisotropy with depth.

5. Discussion

5.1. Broadband Phase Velocity Measurements

[30] We obtained phase velocities of both Rayleigh and Love waves beneath the SB (7–29 s) by analyzing both vertical and horizontal components of BBOBSs. The use of the horizontal component is important not only for analyzing Love waves but also for analyzing first higher-mode Rayleigh waves. The amplitude of the first higher-mode Rayleigh waves in the vertical component is too small to be analyzed in our study (Figure 3), though that in the radial component is large enough to be analyzed. In contrast, both fundamental and first higher modes are clearly observed in the vertical component in EPR regions [*Harmon et al.*, 2007; *Yao et al.*, 2011]. These differences in vertical components

may be reflecting the difference between shallow structures such as the velocity and thickness of shallow crustal layers [e.g., *Tanimoto and Alvizuri*, 2006]. For more detailed discussion, we need to consider the excitation of two modes and the sensitivity of amplitude ratio to the structure in oceanic regions, which is beyond the scope of this study.

[31] At longer periods, we analyzed teleseismic waveforms, and obtained phase velocities for both Rayleigh (29–117 s) and Love (29–59 s) waves. The longest period of observed Love waves is longer in our study than in previous studies [e.g., *Dunn and Forsyth*, 2003] probably because horizontal components of our BBOBS instruments have lower noise level.

5.2. Comparison With Previous Models

[32] We obtained a one-dimensional radially anisotropic structure for the uppermost mantle using average phase velocities of surface waves in the array area. One-dimensional structure can be considered as the lateral and azimuthal average of the three-dimensional anisotropic structure [*Dziewonski and Anderson*, 1981]. Although the trade-off between lateral heterogeneity and azimuthal anisotropy usually exists, the trade-off between lateral heterogeneity and radial anisotropy only exists when the coupling between Rayleigh and Love waves occurs due to the presence of azimuthal anisotropy [*Kawasaki and Koketsu*, 1990]. For the surface waves analyzed in this study, coupling may occur between first higher-mode Rayleigh and fundamental-mode Love waves at periods of 7–9 s, where the phase and group velocities of these waves are similar. However, in the SB region the effect of coupling is expected to be small because the absence of strong Pn anisotropy [*Nishizawa et al.*, 2011] implies that little azimuthal anisotropy exists at depths shallower than 30 km, where surface waves at periods of 7–9 s are sensitive to *S* wave velocity. Therefore, our structural model most likely represents an azimuthal average of the three-dimensional structure beneath the SB.

[33] The presence of crustal heterogeneity in the SB may lead to an incorrect interpretation of the crustal and uppermost mantle structure at depths shallower than ~20 km. Although we simply assumed a crustal thickness of 6 km during the structural inversion, the thickness in the SB determined by refraction surveys is not constant, varying in the range of 4.0–7.5 km, apart from sites of small seamounts that have a crustal thickness of up to 15 km [*Nishizawa et al.*, 2011]. The structure we obtained at depths shallower than 20 km is therefore influenced by both crustal and uppermost mantle structures and needs to be considered with caution. As we are interested in the structure related to LID and LVZ in this study, we mainly interpret the uppermost mantle structure at depths deeper than 20 km. It should be, however, noted that our estimation of *P* wave velocity just below the Moho, 7.8–8.0 km/s, is almost consistent with the Pn velocity estimated by refraction survey, 7.9–8.1 km/s [*Nishizawa et al.*, 2011].

[34] The presence of lateral heterogeneity in the uppermost mantle around the SB may also cause an incorrect structural interpretation. *Isse et al.* [2009] found three slow velocity anomalies in the mantle wedge along the IBM arc at depths of ~50–100 km. The northernmost anomaly is sited beneath the northeastern-most station used in this study, and may affect the average phase velocities in the SB. This effect is, however, expected to be small as the phase velocities obtained from five stations in the southern part of SB are consistent (within the error bar) with the phase velocities obtained from seven stations. At depths greater than 100 km, the presence of the subducting Pacific Plate cannot be neglected as shown in the three-dimensional model of *Isse et al.* [2009]. As such, we avoid comparing structural models at this depth range with thermal models for oceanic basins.

[35] Our final model SB-RA10 shows strong vertical variation (Figure 7b). V_{SV} is greater than 4.5 km/s at depths of 10–40 km, and less than 4.3 km/s at depths of 60–150 km. *Isse et al.* [2010] previously obtained a three-dimensional model in the Philippine Sea region, including azimuthal and radial anisotropy, using fundamental-mode Rayleigh and Love waves at periods of 40–167 s. The period range of *Isse et al.* [2010] is longer than that of our study, and they obtained a smoother V_{SV} model beneath the SB, with an almost constant value of 4.3–4.4 km/s at depths of 10–220 km. We compared the phase velocities given by our structural model and that of *Isse et al.* [2010]. While the differences are less than 1% for fundamental-mode Rayleigh waves at periods longer than 30 s, the differences are 2%–4% for fundamental-mode and first higher-mode Rayleigh waves at shorter periods. This suggests that we need to use phase velocities at periods shorter than 30 s for determining which structural model is closest to the actual structure. The phase velocities measured in this study suggest that our model is more representative of the actual structure. The V_{SH} structure obtained in this study is also different from that of *Isse et al.* [2010]. Our model has V_{SH} higher than 4.7 km/s at depths of 10–40 km, and lower than 4.5 km/s at greater depths, whereas the model of *Isse et al.* [2010] has an almost constant V_{SH} of 4.4–4.6 km/s. This discrepancy reflects differences in the phase velocities of fundamental-mode Love waves. The phase velocity obtained in this study is ~2%–3% higher than the value obtained by *Isse et al.* [2010], which we attribute to damping and smoothing related effects in their analysis.

5.3. LID, LVZ, and the Transition Zone

[36] Since the discovery of the LVZ in the 1950s [*Press*, 1959], the presence of an overlying LID with a constant velocity has been assumed in structural inversions of surface waves to resolve the LVZ beneath oceanic basins [e.g., *Leeds et al.*, 1974; *Schlue and Knopoff*, 1976]. In this study, by conducting broadband surface wave analysis, we obtained a similar structure (SB-RA10; Figure 7b), even when maintaining a uniform structure by introducing a smoothing parameter. This indicates that in situ broadband surface wave dispersion studies utilizing BBOBSs effectively constrain the uppermost mantle structure beneath the oceanic basins related to plate tectonics.

[37] The thickness of the LID is difficult to quantify due to the gradual transition from the LID to LVZ at depths of 40–70 km. We therefore estimated the possible range of the depth and thickness of the LID-LVZ transition zone (LLTZ). In addition, we estimated the velocity gradient in the LID because the almost constant velocity gradient in our final model (Figure 7b) is inconsistent with the negative velocity gradient predicted from the thermal gradient in the uppermost mantle [e.g., *Shapiro and Ritzwoller*, 2004; *Faul and*

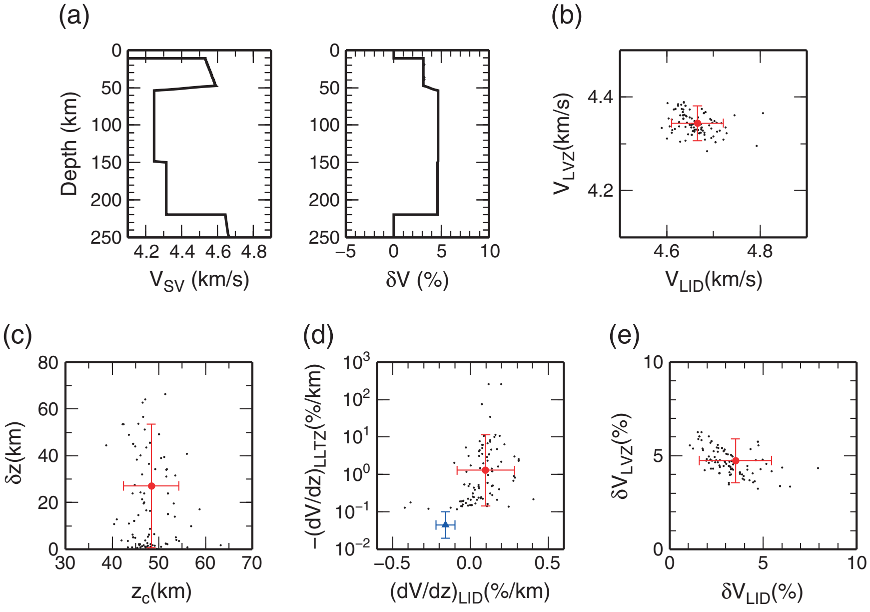

Figure 8. (a) A structure with a LID, LVZ, and LLTZ obtained using the bootstrap average of phase velocity measurements. (b–e) Gray dots show the distributions of the seven model parameters (V_{LID}, V_{LVZ}, z_c, δz, $(\mathrm{d}V/\mathrm{d}z)_{\mathrm{LID}}$, δV_{LID}, δV_{LVZ}, and a parameter calculated from model parameters [$(\mathrm{d}V/\mathrm{d}z)_{\mathrm{LVZ}}$]) for 100 models corresponding to 100 combinations of dispersion curves. Red circles with error bars show the uncertainty range defined by the range of 90 models. A blue triangle with error bar in Figure 8d shows the range predicted by thermal models.

Jackson, 2005]. We also separately estimated the intensity of radial anisotropy in the LID and LVZ to examine possible differences in radial anisotropy. For estimating these parameters, we describe the uppermost mantle structure with seven parameters: center depth and thickness of LLTZ (z_c and δz); average velocity in the LID and LVZ ($V_{\mathrm{LID}} = (V_{SV}^{\mathrm{LID}}+V_{SH}^{\mathrm{LID}})/2$ and $V_{\mathrm{LVZ}} = (V_{SV}^{\mathrm{LVZ}} + V_{SH}^{\mathrm{LVZ}})/2$); velocity gradient in the LID ($(\mathrm{d}V/\mathrm{d}z)_{\mathrm{LID}}$); *S* wave anisotropy in the LID and LVZ (δV_{LID} and δV_{LVZ}). These values can be used to estimate the velocity gradient in the LLTZ ($(dV/dz)_{\mathrm{LLTZ}}$). The depth of the ocean and V_{SV} at depths of 150–220 km are fixed to the values of model SB-RA10.

[38] Figure 8a shows the structure obtained when we used the bootstrap average of phase velocity measurement ($\bar{c}_\gamma$) as data. The uncertainty range of each parameter is further estimated by obtaining 100 models where the lth model is obtained using combinations of lth dispersion curves (c_Z^l, c_R^l, c_T^l, $c_{Z'}^l$, and $c_{T'}^l$) derived by the bootstrap methods. Figures 8b–8e show the distribution of 100 models and the uncertainty range defined by the 90% confidence interval. The average velocity in the LID is $V_{\mathrm{LID}} = 4.6$–4.7 km/s, which is ~7% higher than that in the LVZ ($V_{\mathrm{LVZ}} = 4.3$–4.4 km/s) (Figure 8b). The LLTZ exists at a depth of $z_c = 42$–54 km with a thickness (δz) less than 54 km (Figure 8c). These values are consistent with the G-discontinuity beneath the northern part of the SB observed by *Tonegawa and Helffrich* [2012]. These authors analyzed shear wave reflections and found a velocity drop greater than 6% at depths of 50–70 km with a thickness less than 10 km.

[39] The velocity gradient in the LID ($(\mathrm{d}V/\mathrm{d}z)_{\mathrm{LID}}$) is estimated to be –0.1%/km to 0.3%/km, while that in the LLTZ ($-(\mathrm{d}V/\mathrm{d}z)_{\mathrm{LLTZ}}$) is 0.1–10 %/km (Figure 8d). To compare the obtained velocity gradients with thermal models, we predicted the velocity gradients based on half space cooling models [e.g., *Davis and Lister*, 1974] with various combinations of parameters: seafloor age of 15–30 Ma; thermal diffusivity of 10^{-6} m^2/s; ridge temperature of 1200–1700°C [*Stein and Stein*, 1992]; z_c of 45–55 km; δz of 5–40 km. The temperature gradient in the LID is calculated to be 18–41 K/km. Using temperature and pressure relationships for polycrystalline olivine [*Liu et al.*, 2005], we predict that the velocity gradient in the LID is between –0.23 and –0.09%/km, which lower with a small overlap than the range estimated from phase velocity measurements. One possible cause for this difference is crustal heterogeneity in the SB. Another possible cause relates to the phase transition from plagioclase peridotite to pyroxene peridotite at depths of ~30 km [*Forsyth and Press*, 1971] and/or the presence of orthopyroxene whose pressure and temperature dependence is different from that of olivine at depths shallower than ~40 km. *Stixrude and Lithgow-Bertelloni* [2005] solved the equilibrium equation for a realistic mantle composition and calculated a velocity model based on the half-space cooling model. Their model indicates that the effects of the phase transition and the presence of orthopyroxene is difficult to identify from surface-wave velocities, but may produce velocity gradients in the LID about 0.14 %/km higher than the pure olivine model. The velocity gradient of a realistic mantle model is then between –0.09 and 0.05%/km, which is at the lower end of the 90% confidence interval estimated from our surface-wave velocities.

[40] In contrast, the temperature gradient in the LLTZ is estimated to be 8–20 K/km from the half space cooling models. The corresponding velocity gradient is then

$-(dV/dz)_{\mathrm{LLTZ}}$ = 0.02–0.10 %/km (Figure 8d). If we use more realistic values of the ridge temperature, 1300–1500°C [*Anderson*, 2000], then the gradient is between 0.025 and 0.085%/km. If we consider the realistic mantle composition [*Stixrude and Lithgow-Bertelloni*, 2005], the phase transition from orthopyroxene and spinel to garnet at a depth of ~60 km may decrease the gradient of thermal models. All these cases suggest that the observed velocity gradient is higher than the values predicted from the thermal models. We need to invoke mechanisms for producing this velocity reduction in the LLTZ in addition to the thermal effect, such as decreasing grain size [*Faul and Jackson*, 2005], partial melting [*Anderson and Sammis*, 1970; *Kawakatsu et al.*, 2009], or the presence of water [*Karato*, 2012] in the LVZ. The sharp velocity decrease observed by *Tonegawa and Helffrich* [2012] may require mechanisms such as partial melting or the presence of water. *Baba et al.* [2010] also found a conductivity increase at a depth of ~50 km beneath the SB, and attributed it to the existence of water and/or partial melt at depths of 40–80 km. For any of these mechanisms, the viscosity within the LID is expected to be higher than that in the LVZ [*Fischer et al.*, 2010]. We therefore interpret the LID to be the lithosphere, the LVZ to be the asthenosphere, and the LLTZ to be the lithosphere-asthenosphere boundary (LAB) region.

5.4. Possible Depth Changes in Radial Anisotropy

[41] Our final model (SB-RA10) shows that V_{SH} is 4%–5% larger than V_{SV}. This type of radial anisotropy is conventionally interpreted to be due to olivine LPO and/or the presence of thin layers or pockets of melt. During horizontal shearing, the fast axes (a-axes) of olivine crystals align along the horizontal flow direction and/or the slow axes (b-axes) align vertically, leading to the azimuthal average of V_{SH} becoming faster than V_{SV} [*Estey and Douglas*, 1986]. Some studies have concluded that the presence of thin layers or pockets of partial melt cause radial anisotropy at wavelengths longer than the structure [e.g., *Backus*, 1962; *Forsyth*, 1975; *Schlue and Knopoff*, 1976]. Although the melt distribution tends to dip from the horizontal slip plane under shear stress in laboratory experiments, melt can concentrate along the slip plane if the olivine b-planes are aligned along the slip plane due to the formation of LPO [*Kohlstedt and Zimmerman*, 1996].

[42] For several decades, a number of investigations have focused on examining vertical variations in radial anisotropy [e.g., *Schlue and Knopoff*, 1976; *Cara and Lévêque*, 1988]. Although we attempted to determine the depth dependence of radial anisotropy using broadband surface waves, a structure with constant anisotropy can almost completely explain the phase velocity measurements (Figure 7d). Amplitude difference of anisotropy in the LID and LVZ is difficult to estimate due to a tradeoff between the two parameters as evidenced by the negative trend in Figure 8e. However, the distribution of anisotropy in the LID and LVZ indicates the possibility of greater anisotropy in the LVZ than in the LID. The uncertainty range of $\delta V_{\mathrm{LVZ}} - \delta V_{\mathrm{LID}}$ is –1% to 4%. This result is consistent with the large radial anisotropy identified within the LVZ beneath oceanic basins by tomographic studies [*Ekström and Dziewonski*, 1998; *Nettles and Dziewonski*, 2008]. The stronger radial anisotropy in the LVZ can be interpreted to result from the presence of thin layers or pockets of partial melt in the asthenosphere [*Schlue and Knopoff*, 1976; *Kawakatsu et al.*, 2009], or by enhanced LPO due to strain accumulation in the asthenosphere [*Podolefsky et al.*, 2004; *Becker et al.*, 2008; *Behn et al.*, 2009]. However, in order to determine the change of radial anisotropy at depths shallower than 100 km, we need to analyze the first higher-mode Love wave at periods shorter than 25 s as indicated by the sensitivity kernel in Figure 2c.

6. Conclusions

[43] Using three-component data recorded by seven BBOBSs, we have measured broad period range (7–117 s) Rayleigh and Love wave phase-velocities beneath the SB by noise correlation (< 29 s) and teleseismic surface wave array analysis (> 29 s) (Table 1). This has enabled us to determine the one-dimensional radially anisotropic structure beneath the SB. This structural model has identified the LID at depths shallower than 40 km and the LVZ at depths greater than 70 km. Differences in *S* wave velocities of ~ 6%–10% between the LID and LVZ indicate that they correspond to the lithosphere and asthenosphere, respectively. We also obtained the radial anisotropy with V_{SH} found to be 4%–5% higher than V_{SV}. Although a constant intensity of the radial anisotropy can fit the measured phase velocities, the intensity of radial anisotropy in the LVZ may be higher than that in the LID.

Appendix A: Uncertainties of the Cross Spectra

[44] The propagation of surface waves can be obtained by cross-correlating continuous records of ambient noise [*Shapiro and Campillo*, 2004], which contain both signal (background surface waves) and noise components. The noise is produced by local phenomena such as oceanic currents, and is incoherent with other stations. The noise level of the BBOBS record used in this study is higher than the signal level and depends on the site and observation period. The uncertainty of a cross spectrum is expected to be higher for a pair of stations with higher noise levels. We evaluated the uncertainty by expressing the Fourier spectrum of each segment ($f_{j,\gamma}(\omega)$) as a summation of signal ($s_{j,\gamma}(\omega)$) and noise ($n_{j,\gamma}(\omega)$). The cross spectrum between the *i*th pair of stations ($S^{\mathrm{raw}}_{i,\gamma}(\omega)$) obtained by equation (2) can be written as follows:

$$S^{\mathrm{raw}}_{i,\gamma} = \frac{\langle w_{i,\gamma} \cdot s_{j,\gamma} \cdot s^*_{k,\gamma} \rangle}{\langle w_{i,\gamma} \rangle} + \frac{\langle w_{i,\gamma} \cdot s_{j,\gamma} \cdot n^*_{k,\gamma} \rangle}{\langle w_{i,\gamma} \rangle} + \frac{\langle w_{i,\gamma} \cdot n_{j,\gamma} \cdot s^*_{k,\gamma} \rangle}{\langle w_{i,\gamma} \rangle} + \frac{\langle w_{i,\gamma} \cdot n_{j,\gamma} \cdot n^*_{k,\gamma} \rangle}{\langle w_{i,\gamma} \rangle}, \qquad \text{(A1)}$$

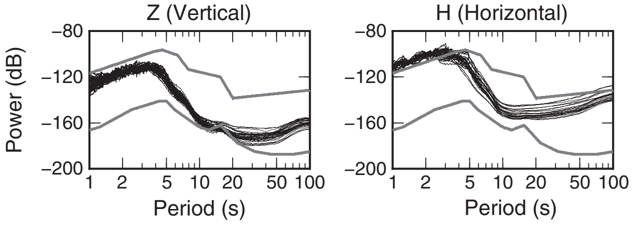

Figure A1. Variation in site-dependent noise level for each pair of stations ($< w_{i,\gamma} >^{-1}$; thin black lines) with the New Low and High Noise Models [*Peterson*, 1993] (thick gray lines).

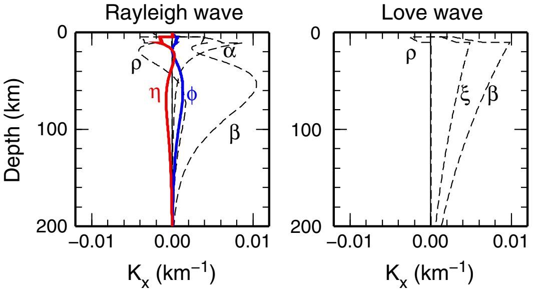

Figure B1. Sensitivity of the parameter p to the phase velocities of fundamental-mode surface waves at a period of 40 s (K_p) for the modified PREM with a crustal thickness of 6 km and a sea depth of 4.6 km.

where $w_{i,\gamma}(\omega) = |\tilde{f}_{j,\gamma}|^{-1} \cdot |\tilde{f}_{k,\gamma}|^{-1}$ is the weighting term for reducing the contribution of the segment with a large noise. When the noise level is much higher than the signal level, the second and third terms are negligible compared with the fourth term. In addition, the amplitude of the numerator of the fourth term is almost one ($w_{i,\gamma} \cdot n_{j,\gamma} \cdot n^*_{k,\gamma} \sim 1$) before taking the ensemble average and becomes approximately $1/\sqrt{N}$ upon taking the average of N ensembles. The number of ensembles is $N \sim 1$ yr/1638 s $\times 2 \sim 38{,}000$, which is almost constant for all the cross spectra. We therefore obtain

$$S^{\mathrm{raw}}_{i,\gamma} \simeq \frac{\langle w_{i,\gamma} \cdot s_{j,\gamma} \cdot s^*_{k,\gamma} \rangle}{\langle w_{i,\gamma} \rangle} + \frac{1}{\langle w_{i,\gamma} \rangle} \mathcal{O}\left(\frac{1}{\sqrt{N}} \right), \qquad \text{(A2)}$$

where the first and second terms are the signal and uncertainty of each cross spectrum, respectively. The signal level of each cross spectrum is proportional to the source spectrum (s^2), whereas the uncertainty is proportional to $\langle w_{i,\gamma} \rangle^{-1} \sim |\tilde{f}_{j,\gamma}| \cdot |\tilde{f}_{k,\gamma}|$, which is the product of noise levels at the jth and kth stations. Figure A1 shows the actual value of $\langle w_{i,\gamma} \rangle^{-1}$. The noise level of one pair of stations differs from others by up to a factor of 100. The variation in uncertainties of cross spectra is therefore large. In order to reduce the contribution of cross spectra with large uncertainty, we used a weighting term during the fitting of each cross spectrum to the theoretical equation as shown in equation (7).

Appendix B: Anisotropic Parameter Scalings

[45] Eight parameters are used to describe radially anisotropic media: density (ρ); two attenuation coefficients; two velocity parameters; $\alpha = V_{PH}$ and $\beta = V_{SV}$; and three anisotropic parameters ($\xi = N/L = (V_{SH}/V_{SV})^2$, $\phi = C/A = (V_{PV}/V_{PH})^2$, and $\eta = F/(A - 2L)$) [*Takeuchi and Saito*, 1972]. Figure B1 shows sensitivity kernels of phase velocities for each parameter for a model based on PREM [*Dziewonski and Anderson*, 1981]. We could not recognize the sensitivity of Rayleigh waves to ξ and the sensitivity of Love waves to α, ϕ, and η because they are zero or almost zero. The most important relationship is that the sensitivity of Rayleigh waves to ϕ and η are the negative of each other. As a result, $\phi + \eta$ has almost no effect on the phase velocity, whereas $\phi - \eta$ has a minor effect. It is necessary to constrain $\phi - \eta$ with an accuracy of 10% for estimating β and $\delta V = \sqrt{\xi} - 1$ with an accuracy of 1%.

[46] *Montagner and Anderson* [1989] first discussed the correlations between anisotropic parameters when the mantle has an LPO. Their results for olivine can be parameterized as follows:

$$\phi \sim \xi^{-1.5}, \quad \eta \sim \xi^{-2.5}, \qquad \text{(B1)}$$

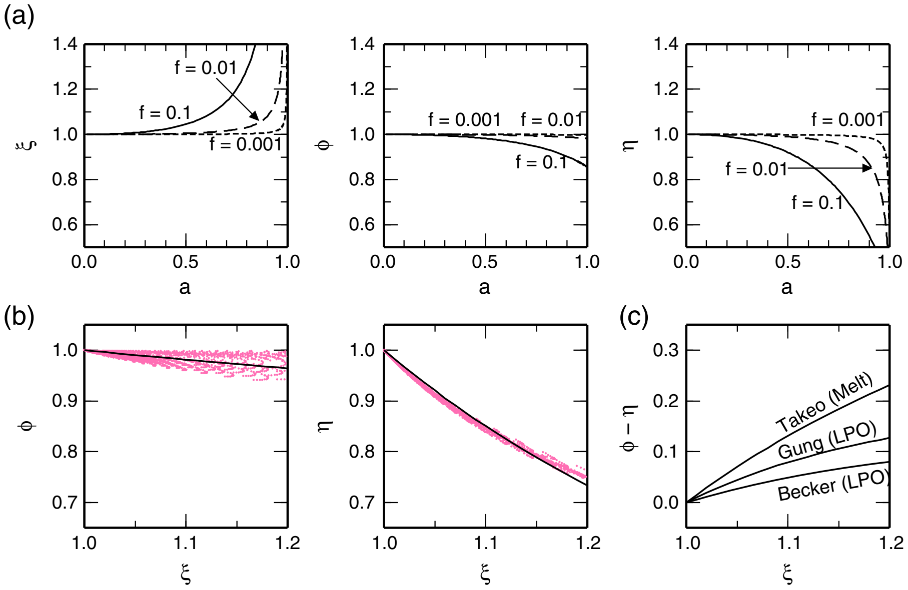

Figure B2. (a) Anisotropic parameters for a simple melt layering model when b is set to 0.5. (b) Correlation between anisotropic parameters in the simple melt layering model. Each dot indicates a combination of three anisotropic parameters (a, b, and f). The fitted curves are shown by solid lines. (c) Correlation between $\phi - \eta$ and ξ for three different scaling relationships (*Gung et al.* [2003], *Becker et al.* [2008], and this study).

following *Gung et al.* [2003]. *Becker et al.* [2008] also considered this topic and obtained a different relationship:

$$\phi \sim \xi^{-1.4}, \quad \eta \sim \xi^{-2.0}, \tag{B2}$$

by considering a mixture of olivine and enstatite crystals. These equations show that P wave anisotropy is larger than S wave anisotropy. However, if radial anisotropy is caused by the presence of pockets or layers of partial melt, then the S wave anisotropy should be larger than the P wave anisotropy, because the velocity reduction caused by melting is greater for S waves than for P waves. We obtained a new relationship when anisotropy originates from melt layering. This calculation is based on a simple melt layering model in which layers of partial melt are horizontal and thin as compared with the surrounding solid rock layers. Such a model can be represented using three parameters: (i) the reduction of rigidity in layers containing partial melt as compared with the rock layers (a); (ii) the reduction of the bulk modulus as compared with the reduction in rigidity (b); and (iii) the thickness of layers containing partial melt as compared with that of the rock layers (f). The Poisson ratio is set to 0.25 for melt-free layers. By varying combinations of these parameters between $0 < a < 1$, $0.4 < b < 0.6$, and $0 < f < 0.1$, we calculated long wavelength equivalent elastic constants with the formulation of *Backus* [1962]. Figure B2a shows three anisotropic parameters for $b = 0.5$, and Figure B2b shows the correlations between these parameters. We scaled these parameters using the following:

$$\phi \sim \xi^{-0.2}, \quad \eta \sim \xi^{-1.7}. \tag{B3}$$

Figure B2c summarizes the relationship between $\phi - \eta$ and ξ for three scaling relationships. As already noted, it is necessary to constrain $\phi - \eta$ to an accuracy of 10% in order to obtain β and $\delta V = \sqrt{\xi} - 1$ with an accuracy of 1%. The scaling method of *Gung et al.* [2003] is suitable for this purpose because the difference of $\phi - \eta$ between the scaling and other scalings are smaller than 10% ($\xi < 1.2$).

[47] **Acknowledgments.** We thank two anonymous reviewers, the associate editor, and the editor Robert Nowack for the patience and the constructive comments that significantly improved the quality of the manuscript. This work was supported by Grant-in-Aids for JSPS Fellows (23-8157) and Scientific Research (16075203, 22000003, 24654142). We used GMT [*Wessel and Smith*, 1991] and SAC2000 [*Goldstein and Snoke*, 2005] software during this study.

References

Aki, K. (1957), Space and time spectra of stationary stochastic waves, with special reference to microtremors, *Bull. Earthquake Res. Inst.*, *35*(3), 415–456.

Aki, K., and K. Kaminuma (1963), Phase velocity of low waves in Japan (Part 1): Love waves from the Aleutian Shock of March 9, 1957, *Bull. Earthquake Res. Inst.*, *41*(1), 243–259.

Anderson, D. L. (1962), Love wave dispersion in heterogeneous anisotropic media, *Geophysics*, *27*(4), 445–454, doi:10.1190/1.1.439042.

Anderson, D. L. (2000), The thermal state of the upper mantle: No role for mantle plumes, *Geophys. Res. Lett.*, *27*(22), 3623–3626, doi:10.1029/2000GL011533.

Anderson, D. L., and J. D. Bass (1984), Mineralogy and composition of the upper mantle, *Geophys. Res. Lett.*, *11*(7), 637–640, doi:10.1029/GL011i007p00637.

Anderson, D. L., and C. Sammis (1970), Partial melting in the upper mantle, *Phys. Earth Planet. Inter.*, *3*, 41–50, doi:10.1016/0031-9201(70)90042-7.

Baba, K., H. Utada, T. Goto, T. Kasaya, H. Shimizu, and N. Tada (2010), Electrical conductivity imaging of the Philippine Sea upper mantle using seafloor magnetotelluric data, *Phys. Earth Planet. Inter.*, *183*(1-2), 44–62, doi:10.1016/j.pepi.2010.09.010.

Backus, G. E. (1962), Long-wave elastic anisotropy produced by horizontal layering, *J. Geophys. Res.*, *67*(11), 4427–4440, doi:10.1029/JZ067i011p04427.

Becker, T. W., B. Kustowski, and G. Ekström (2008), Radial seismic anisotropy as a constraint for upper mantle rheology, *Earth Planet. Sci. Lett.*, *267*(1-2), 213–227, doi:10.1016/j.epsl.2007.11.038.

Behn, M. D., G. Hirth, and J. R. Elsenbeck II (2009), Implications of grain size evolution on the seismic structure of the oceanic upper mantle, *Earth Planet. Sci. Lett.*, *282*(1-4), 178–189, doi:10.1016/j.epsl.2009.03.014.

Bensen, G. D., M. H. Ritzwoller, M. P. Barmin, a. L. Levshin, F. Lin, M. P. Moschetti, N. M. Shapiro, and Y. Yang (2007), Processing seismic ambient noise data to obtain reliable broad-band surface wave dispersion measurements, *Geophys. J. Int.*, *169*(3), 1239–1260, doi:10.1111/j.1365-246X.2007.03374.x.

Bensen, G. D., M. H. Ritzwoller, and N. M. Shapiro (2008), Broadband ambient noise surface wave tomography across the United States, *J. Geophys. Res.*, *113*, B05306, doi:10.1029/2007JB005248.

Bozdag, E., and J. Trampert (2008), On crustal corrections in surface wave tomography, *Geophys. J. Int.*, *172*(3), 1066–1082, doi:10.1111/j.1365-246X.2007.03690.x.

Cara, M., and J. J. Lévêque (1988), Anisotropy of the asthenosphere: The higher mode data of the Pacific revisited, *Geophys. Res. Lett.*, *15*(3), 205–208, doi:10.1029/GL015i003p00205.

Christensen, N. I., and M. H. Salisbury (1975), Structure and constitution of the lower oceanic crust, *Rev. Geophys.*, *13*(1), 57–86, doi:10.1029/RG013i001p00057.

Cox, H. (1973), Spatial correlation in arbitrary noise fields with application to ambient sea noise, *J. Acoust. Soc. Am.*, *54*(5), 1289–1301, doi:10.1121/1.1.914426.

Davis, E., and C. Lister (1974), Fundamentals of ridge crest topography, *Earth Planet. Sci. Lett.*, *21*(4), 405–413, doi:10.1016/0012-821X(74)90180-0.

Dorman, J., M. Ewing, and J. Oliver (1960), Study of shear-velocity distribution in the upper mantle by mantle Rayleigh waves, *Bull. Seismol. Soc. Am.*, *50*(1), 87–115.

Dunn, R. A., and D. W. Forsyth (2003), Imaging the transition between the region of mantle melt generation and the crustal magma chamber beneath the southern East Pacific Rise with short-period Love waves, *J. Geophys. Res.*, *108*(B7), 2352, doi:10.1029/2002JB002217.

Dziewonski, A. M., and D. L. Anderson (1981), Preliminary reference Earth model, *Phys. Earth Planet. Inter.*, *25*(4), 297–356, doi:10.1016/0031-9201(81)90046-7.

Efron, B. (1979), Bootstrap methods: Another look at the jackknife, *Ann. Stat.*, *7*(1), 1–26, doi:10.1214/aos/1176344552.

Ekström, G., and A. M. Dziewonski (1998), The unique anisotropy of the Pacific upper mantle, *Nature*, *394*(6689), 168–172, doi:10.1038/28148.

Ekström, G., G. A. Abers, and S. C. Webb (2009), Determination of surface-wave phase velocities across USArray from noise and Aki's spectral formulation, *Geophys. Res. Lett.*, *36*(18), 5–9, doi:10.1029/2009GL039131.

Estey, L. H., and B. J. Douglas (1986), Upper mantle anisotropy: A preliminary model, *J. Geophys. Res.*, *91*(B11), 11,393–11,406, doi:10.1029/JB091iB11p11393.

Ewing, W. M., W. S. Jardetzky, and F. Press (1957), *Elastic Waves in Layered Media*, 380 pp., McGraw Hill, New York.

Faul, U. H., and I. Jackson (2005), The seismological signature of temperature and grain size variations in the upper mantle, *Earth Planet. Sci. Lett.*, *234*, 119–134, doi:10.1029/2001JB001225.

Fischer, K. M., H. A. Ford, D. L. Abt, and C. A. Rychert (2010), The lithosphere-asthenosphere boundary, *Annu. Rev. Earth Planet. Sci.*, *38*(1), 551–575, doi:10.1146/annurev-earth-040809-152438.

Forsyth, D. W. (1975), The early structural evolution and anisotropy of the oceanic upper mantle, *Geophys. J. Int.*, *43*(1), 103–162, doi:10.1111/j.1365-246X.1975.tb00630.x.

Forsyth, D. W., and A. Li (2005), Array Analysis of two-dimensional variations in surface wave phase velocity and azimuthal anisotropy in the presence of multipathing interference, in *Seismic Earth: Array Analysis of Broadband Seismograms, Geophys. Monogr. Ser.,* vol. 157, pp. 81–97, AGU, Washington D. C.

Forsyth, D. W., and F. Press (1971), Geophysical tests of petrological models of the spreading lithosphere, *J. Geophys. Res.*, *76* (32), 7963–7979, doi:10.1029/JB076i032p07963.

Gaherty, J. B., T. H. Jordan, and L. S. Gee (1996), Seismic structure of the upper mantle in a central Pacific corridor, *J. Geophys. Res.*, *101*(B10), 22,291–22,309, doi:10.1029/96JB01882.

Goldstein, P., and A. Snoke (2005), SAC availability for the IRIS community, *DMS Electron. Newsl.*, *7*(1), Feature Article. [Available at http://www.iris.edu/dms/newsletter/].

Gung, Y., M. Panning, and B. Romanowicz (2003), Global anisotropy and the thickness of continents, *Nature*, *422*(April), 707–711, doi:10.1038/nature01557.1.

Gutenberg, B. (1959), Wave velocities below the Mohorovicic discontinuity, *Geophys. J. Int.*, *2*(4), 348–352, doi:10.1111/j.1365-246X.1959.tb05805.x.

Harmon, N., D. Forsyth, and S. Webb (2007), Using ambient seismic noise to determine short-period phase velocities and shallow shear velocities in young oceanic lithosphere, *Bull. Seismol. Soc. Am.*, *97*(6), 2009–2023, doi:10.1785/0120070050.

Ingber, L. (1989), Very fast simulated re-annealing, *Math. Comput. Model.*, *12*(8), 967–973, doi:10.1016/0895-7177(89)90202-1.

Isse, T., H. Shiobara, Y. Tamura, D. Suetsugu, K. Yoshizawa, H. Sugioka, A. Ito, T. Kanazawa, M. Shinohara, and K. Mochizuki (2009), Seismic structure of the upper mantle beneath the Philippine Sea from seafloor and land observation: Implications for mantle convection and magma genesis in the Izu-Bonin-Mariana subduction zone, *Earth Planet. Sci. Lett.*, *278*(1-2), 107–119, doi:10.1016/j.epsl.2008.11.032.

Isse, T., H. Shiobara, J.-P. Montagner, H. Sugioka, A. Ito, A. Shito, T. Kanazawa, and K. Yoshizawa (2010), Anisotropic structures of the upper mantle beneath the northern Philippine Sea region from Rayleigh and Love wave tomography, *Phys. Earth Planet. Inter.*, *183* (1-2), 33–43, doi:10.1016/j.pepi.2010.04.006.

Kanamori, H., and D. L. Anderson (1977), Importance of physical dispersion in surface wave and free oscillation problems: Review, *Rev. Geophys.*, *15*(1), 105–112, doi:10.1029/RG015i001p00105.

Kanazawa, T., M. Shinohara, and H. Shiobara (2009), Recent progress in seafloor earthquake observations and instruments in Japan [in Japanese with English abstract], *J. Seismol. Soc. Jpn*, *61*, S55—S68.

Karato, S.-i. (2012), On the origin of the asthenosphere, *Earth Planet. Sci. Lett.*, *321-322*, 95–103, doi:10.1016/j.epsl.2012.01.001.

Kato, M., and T. H. Jordan (1999), Seismic structure of the upper mantle beneath the western Philippine Sea, *Phys. Earth Planet. Inter.*, *110*(3-4), 263–283, doi:10.1016/S0031-9201(98)00176-9.

Kawakatsu, H., P. Kumar, Y. Takei, M. Shinohara, T. Kanazawa, E. Araki, and K. Suyehiro (2009), Seismic evidence for sharp lithosphere-asthenosphere boundaries of oceanic plates, *Science*, *324* (5926), 499–502, doi:10.1126/science.1169499.

Kawasaki, I., and K. Koketsu (1990), Rayleigh-Love wave coupling in an azimuthally anisotropic medium, *J. Phys. Earth*, *38*(5), 361–390, doi:10.4294/jpe1952.38.361.

Kohlstedt, D. L., and M. E. Zimmerman (1996), Rheology of partially molten mantle rocks, *Annu. Rev. Earth Planet. Sci.*, *24*(1), 41–62, doi:10.1146/annurev.earth.24.1.41.

Leeds, A. R., L. Knopoff, and E. G. Kausel (1974), Variations of upper mantle structure under the Pacific Ocean, *Science*, *186*(4159), 141–143, doi:10.1126/science.186.4159.141.

Liu, W., J. Kung, and B. Li (2005), Elasticity of San Carlos olivine to 8 GPa and 1073 K, *Geophys. Res. Lett.*, *32*, L16301, doi:10.1029/2005GL023453.

Maggi, A., E. Debayle, K. Priestley, and G. Barruol (2006), Multimode surface waveform tomography of the Pacific Ocean: A closer look at the lithospheric cooling signature, *Geophys. J. Int.*, *166*(3), 1384–1397, doi:10.1111/j.1365-246X.2006.03037.x.

Montagner, J.-P., and D. L. Anderson (1989), Petrological constraints on seismic anisotropy, *Phys. Earth Planet. Inter.*, *54*(1-2), 82–105, doi:10.1016/0031-9201(89)90189-1.

Nakahara, H. (2006), A systematic study of theoretical relations between spatial correlation and Green's function in one-, two- and three-dimensional random scalar wavefields, *Geophys. J. Int.*, *167*(3), 1097–1105, doi:10.1111/j.1365-246X.2006.03170.x.

Nakamura, Y., and T. Shibutani (1998), Three-dimensional shear wave velocity structure in the upper mantle beneath the Philippine Sea region, *Earth Planets Space*, *50*, 939–952.

Nettles, M., and A. M. Dziewonski (2008), Radially anisotropic shear velocity structure of the upper mantle globally and beneath North America, *J. Geophys. Res.*, *113*, B02303, doi:10.1029/2006JB004819.

Nishida, K. (2011), Two-dimensional sensitivity kernels for cross-correlation functions of background surface waves, *C. R. Geosci.*, *343*(8-9), 584–590, doi:10.1016/j.crte.2011.02.004.

Nishida, K., H. Kawakatsu, and K. Obara (2008), Three-dimensional crustal *S* wave velocity structure in Japan using microseismic data recorded by Hi-net tiltmeters, *J. Geophys. Res.*, *113*, B10302, doi:10.1029/2007JB005395.

Nishizawa, A., K. Kaneda, and M. Oikawa (2011), Backarc basin oceanic crust and uppermost mantle seismic velocity structure of the Shikoku Basin, south of Japan, *Earth Planets Space*, *63*(2), 151–155, doi:10.5047/eps.2010.12.003.

Okino, K., Y. Ohara, S. Kasuga, and Y. Kato (1999), The Philippine Sea: New survey results reveal the structure and the history of the marginal basins, *Geophys. Res. Lett.*, *26*(15), 2287–2290, doi:10.1029/1999GL900537.

Peterson, J., (1993), Observations and modeling of seismic background noise, *Tech. rep., U.S. Geol. Surv. Open File Rep., 93–322*.

Podolefsky, N. S., S. Zhong, and A. K. McNamara (2004), The anisotropic and rheological structure of the oceanic upper mantle from a simple model of plate shear, *Geophys. J. Int.*, *158*(1), 287–296, doi:10.1111/j.1365-246X.2004.02250.x.

Press, F. (1959), Some implications on mantle and crustal structure from G waves and Love waves, *J. Geophys. Res.*, *64*(5), 565–568, doi:10.1029/JZ064i005p00565.

Revenaugh, J., and T. H. Jordan (1991), Mantle layering from ScS reverberations: 2. The transition zone, *J. Geophys. Res.*, *96*(B12), 19,763–19,780, doi:10.1029/91JB01486.

Ritzwoller, M. H., N. M. Shapiro, and S.-J. Zhong (2004), Cooling history of the Pacific lithosphere, *Earth Planet. Sci. Lett.*, *226*(1-2), 69–84, doi:10.1016/j.epsl.2004.07.032.

Rychert, C. a., and P. M. Shearer (2011), Imaging the lithosphere-asthenosphere boundary beneath the Pacific using SS waveform modeling, *J. Geophys. Res.*, *116*, B07307, doi:10.1029/2010JB008070.

Saito, M. (1988), DISPER80: A subroutine package for the calculation of seismic normal-mode solutions, in *Seismological Algorithms*, pp. 293–319, Academic, San Diego, Calif.

Schlue, J. W., and L. Knopoff (1976), Shear wave anisotropy in the upper mantle of the Pacific Basin, *Geophys. Res. Lett.*, *3*(6), 359–362, doi:10.1029/GL003i006p00359.

Shapiro, N. M., and M. Campillo (2004), Emergence of broadband Rayleigh waves from correlations of the ambient seismic noise, *Geophys. Res. Lett.*, *31*, L07614, doi:10.1029/2004GL019491.

Shapiro, N. M., and M. H. Ritzwoller (2004), Thermodynamic constraints on seismic inversions, *Geophys. J. Int.*, *157*(3), 1175–1188, doi:10.1111/j.1365-246X.2004.02254.x.

Shinohara, M., T. Fukano, T. Kanazawa, E. Araki, K. Suyehiro, M. Mochizuki, K. Nakahigashi, T. Yamada, and K. Mochizuki (2008), Upper mantle and crustal seismic structure beneath the Northwestern Pacific Basin using a seafloor borehole broadband seismometer and ocean bottom seismometers, *Phys. Earth Planet. Inter.*, *170* (1-2), 95–106, doi:10.1016/j.pepi.2008.07.039.

Shiobara, H., K. Baba, H. Utada, Y. Fukao, N. S. Plan, and R. Taylor (2009), Ocean Bottom array probes stagnant slab beneath the Philippine Sea, *Eos Trans. AGU*, *90*(9), 70–71, doi:10.1029/2009EO090002.

Stein, C. A., and S. Stein (1992), A model for the global variation in oceanic depth and heat flow with lithospheric age, *Nature*, *359*(6391), 123–129, doi:10.1038/359123a0.

Stixrude, L., and C. Lithgow-Bertelloni (2005), Mineralogy and elasticity of the oceanic upper mantle: Origin of the low-velocity zone, *J. Geophys. Res.*, *110*, B03204, doi:10.1029/2004JB002965.

Takeuchi, H., and M. Saito (1972), Seismic surface waves, in *Methods in Computational Physics*, pp. 217–295, Academic Press, New York.

Tanimoto, T., and C. Alvizuri (2006), Inversion of the HZ ratio of microseisms for *S*-wave velocity in the crust, *Geophys. J. Int.*, *165*(1), 323–335, doi:10.1111/j.1365-246X.2006.02905.x.

Tonegawa, T., and G. Helffrich (2012), Basal reflector under the Philippine Sea plate, *Geophys. J. Int.*, *189*, 659–668, doi:10.1111/j.1365-246X.2012.05386.x.

Tromp, J., Y. Luo, S. Hanasoge, and D. Peter (2010), Noise cross-correlation sensitivity kernels, *Geophys. J. Int.*, *183*(2), 791–819, doi:10.1111/j.1365-246X.2010.04721.x.

Weaver, R., B. Froment, and M. Campillo (2009), On the correlation of non-isotropically distributed ballistic scalar diffuse waves, *J. Acoust. Soc. Am.*, *126*(4), 1817–1826, doi:10.1121/1.3203359.

Weeraratne, D. S., D. W. Forsyth, Y. Yang, and S. C. Webb (2007), Rayleigh wave tomography beneath intraplate volcanic ridges in the South Pacific, *J. Geophys. Res.*, *112*, B06303, doi:10.1029/2006JB004403.

Wessel, P., and W. H. F. Smith (1991), Free software helps map and display data, *Eos Trans. AGU*, *72*(41), 441, doi:10.1029/90EO00319.

Yao, H., and R. D. van der Hilst (2009), Analysis of ambient noise energy distribution and phase velocity bias in ambient noise tomography, with application to SE Tibet, *Geophys. J. Int.*, *179*(2), 1113–1132, doi:10.1111/j.1365-246X.2009.04329.x.

Yao, H., P. Gouédard, J. a. Collins, J. J. McGuire, and R. D. van der Hilst (2011), Structure of young East Pacific Rise lithosphere from ambient noise correlation analysis of fundamental- and higher-mode Scholte-Rayleigh waves, *C. R. Geosci.*, *343*, 571–583, doi:10.1016/j.crte.2011.04.004.